scientific data

Check for updates

OPEN

DATA DESCRIPTOR

Model datasets of orographical perturbation experiments for the Mongolian plateau by using CAS FGOALS-f3-L

Nuo Xu[1,2,3], Bian He[2,3,4]✉, Zuowei Xie[2,5], Zhongda Lin[2,3], Shijian Feng[2,3,4], Yimin Liu[2,3,4], Guoxiong Wu[2,3,4], Qing Bao[3], Kangjun Chen[2,3], Natalia Victorovna Vazaeva[6] & Shibo Gao[1]✉

Topography is an important forcing for climate change. Compared to the extensively studies of Tibetan Plateau, the impact of Mongolian Plateau (MP) is less understood. This paper introduces three experiments which examine both the thermal and dynamical effects of the MP and its surrounding areas carried out by the climate model CAS FGOALS-f3-L. Each experiment produces 42 variables, including monthly, daily average, 6-hourly transient, and hourly outputs for precipitation and surface air temperature. The model datasets are all interpolated into nominal 1 degree resolution. The validation results show that the control run can well capture the basic circulation pattern over Eurasian continent, while the model responses to thermal and dynamical perturbations of MP are reasonable. These datasets provide a reference for understanding the response of weather and climate change in the middle and high latitudes to the mechanical and thermal forcing of the MP, and help to understand the contribution of the MP to the monsoon circulation, winter cold waves and even extreme events in the middle and high latitudes.

Background & Summary

The colossal topographies in Asia, exemplified by the Tibetan Plateau (TP), Iranian Plateau (IP) and the Mongolian Plateau (MP), exert a pronounced influence on the climate[1–9]. Previous numerous studies reveal the influences of TP and IP on the changes of Asian weather and climate in various aspects. The thermodynamical forcing of TP could modulate the monsoon systems, affect regional temperature and precipitation patterns by influence the regional land-air-sea interactions[10–12]. The topographic features of the TP play an indispensable role in the formation mechanisms of the Asian monsoon, and its influence on seasonal circulation transitions[13–15].Currently, there is significant attention to the dynamical and thermal effects of the TP on climate. However, research focusing on the climatic impacts of the MP in mid-high latitudes remains relatively limited.

The uplift of the MP is currently considered a byproduct of the partial collision between the Eurasian continent and the Indian subcontinent, serving as a supplement to the formation of the TP[16]. The MP is located in the mid-high latitudes of Asia (37°24′N to 53°12′N, 88°34′E to 126°04′E), spanning Mongolia, northern China, and southern Russia, with an area of approximately 2 million square kilometers. It extends from the Greater Khingan Range in the east to the Altai Mountains in the west. The terrain of the MP gradually slopes downward from west to east, with an average elevation of around 1,500 meters. The region is primarily characterized by

[1]College of Agronomy, Shenyang Agricultural University, Shenyang, China. [2]State Key Laboratory of Earth System Numerical Modeling and Application, Institute of Atmospheric Physics, Chinese Academy of Sciences, Beijing, 100029, China. [3]State Key Laboratory of Numerical Modeling for Atmospheric Sciences and Geophysical Fluid Dynamics (LASG), Institute of Atmospheric Physics (IAP), Chinese Academy of Sciences, Beijing, 100029, China. [4]University of Chinese Academy of Sciences, Beijing, 100029, China. [5]International Center for Climate and Environment Sciences, Institute of Atmospheric Physics, Chinese Academy of Sciences, Beijing, 100029, China. [6]The Laboratory of geophysical hydrodynamics of the A.M. Obukhov Institute of Atmospheric Physics of Russian Academy of Sciences (IAP RAS), Moscow, Russia. ✉e-mail: heb@lasg.iap.ac.cn; sgao@syau.edu.cn

alpine meadow, upland, and deserts, situated in the transitional zone between the East Asian monsoon and the westerlies[17].

Although the MP is considerably smaller in scale and elevation compared to the TP, its location is more northerly and at higher latitude. This unique geographical position that the MP in the core area of the westerly circulation in the Northern Hemisphere. Compared to the main part of TP, the dynamical forcing effect of MP on the upper tropospheric westerly jet is more pronounced[18]. Previous Numerical simulation studies have shown that the uplift of the MP significantly enhances planetary waves in the Northern Hemisphere atmosphere[19,20]. Furthermore, MP plays a significant role in near-surface weather and climate systems. Before the uplift of MP, the Siberian High (SiH) was located in eastern China with relatively weak intensity. After the uplift of MP, SiH shifted northward and intensified, leading to an enhancement of the winter north-westerly wind in East Asia[21,22]. The uplift of the MP also causes the westerly wind belt to shift northward and increases the intensity of the East Asian winter monsoon[19,22]. These studies indicate that even a relatively small terrain can generate substantial dynamical effects due to its specific geographical location. The MP represents a unique topographic forcing in the mid-high latitudes of the Asian continent, with an influence far more extensive than anticipated.

Against the backdrop described above, to establish benchmark experiments for more profound and comprehensive understanding of the MP's forcing on the mid-high latitudes circulation changes, and even extreme weather occurrences, to advance a more mechanistic understanding of how Asian topography modulates the global monsoon system, we have meticulously designed and executed a series of numerical simulation experiments on examining the influences of MP. Compared to the experiments in the Coupled Model Intercomparison Project (CMIP6) Global Monsoons Model Intercomparison Project (GMMIP) Tier3[23], this experiment focuses on examining the thermal and dynamical effects of the MP and its surrounding regions. Reviewing previous numerical simulation experiments aimed at investigating the climatic impact of the MP, they primarily relied on dynamical experimental methods, specifically by applying a "no topography" treatment to MP. However, in this experiment, we have additionally incorporated a thermal experiment related to the MP and adjacent regions, which has not been conducted by previous studies. The overall objective is to provide new numerical simulation experimental data, to further explore the specific impacts of the MP on climate and atmospheric circulation change under the combined influence of dynamical and thermal effects. By doing so, we aim to fill the gaps in previous research work in this field and provide a better understanding of the dynamical and thermal effects of the MP on climate.

Methods

Introduction to numerical model. We use the Chinese Academy of Sciences (CAS) Flexible Global Ocean-Atmosphere-Terrestrial System model, finite-volume version 3 (FGOALS-f3-L) (the 'L' denotes a low nominal resolution of 100 km). The following is a brief introduction to the FGOALS-f3-L model.

The basic structure of FGOALS-f3-L is as follows: the atmospheric component is the Finite-volume Atmospheric Model (FAMIL) version 2.2[24–26], which is an upgraded version of the Spectral Atmosphere Model (SAMIL) of the Next Generation Atmospheric General Circulation Model (AGCM)[27–29]. Ocean component: LASG / IAP Climate System Ocean Mode 3.0 version (LICOM3)[30], with high horizontal resolution and vertical stratification. Land component: Community Land Model (CLM) version 4.0, used to simulate land surface processes. Sea ice composition: Los Alamos Sea Ice Model (CICE4)[31], used to simulate sea ice dynamics.

The grid system of FAMIL adopts a cubic sphere grid system, which contains 6 tiles, each of which contains 96 grids. Globally, the meridional region is divided into 384 grids, and the zonal region is divided into 192 grids, with a horizontal resolution of about $1° \times 1°$. In the vertical direction, 32 layers of mixed coordinates are used, and the top of the mode is 2.16 hPa. The flux exchange between the components of FGOALS-f3-L is carried out through the 7th edition of the National Center for Atmospheric Research (NCAR) Coupler Module.

The model integrates a multi-scale physical process parameterization scheme to optimize the coupled simulation of the climate system. The boundary layer module uses an improved humidity turbulence parameterization scheme[32], combined with the latest correction method for shallow convection processes[33]. Six-hydrometeor classification frameworks based on GFDL (Geophysical Fluid Dynamics Laboratory) for cloud microphysical processes predicted the distribution characteristics of water vapor, cloud water, cloud ice, rain, snow and graupel synchronously through a single-moment scheme[34,35]. The cloud fraction diagnosis module significantly improves the simulation accuracy of cloud phase distribution by integrating relative humidity and cloud mixing ratio parameters[36]. Different from the traditional convective parameterization method, the model introduces an explicit separated cumulus-stratiform precipitation computer mechanism (FAMIL Development Team, 2017) to realize the refined characterization of convective precipitation. In addition, the atmospheric gravity wave drag effect is incorporated into the model energy transfer process through the classical dynamic scheme[37].

Experimental design. To investigate the thermal and dynamical effects of MP, three types of Atmospheric Model Intercomparison Project (amip) runs were conducted, namely the control run (amip), the no mountain run (amip_NMO), and the no sensible heating run (amip_NS_MO). As presented in Table 1, the experiment_id of the three experiments and the configurations of each experiment are provided.

The control run (amip), serving as a reference simulation, starting from January 1, 1976, with the first three years considered as a spin-up time. All external forcing factors, including greenhouse gases, solar irradiance, ozone, and aerosols, are prescribed their historical values. Sea surface temperature (SST) and sea ice concentration are set to observed values. Output data for analysis are provided from January 1, 1979, to December 15, 2021. The second run (amip_NMO) is dynamical perturbation experiment, the height of the topography in the MP and its surrounding regions is modified. The topography above 500 m in the MP and its surrounding regions is set to 500 m. Additionally, other land use and surface properties remain unchanged. The output variables time is the same as the control experiment. The third run is a thermal perturbation experiment (amip_NS_MO). In

Experiment_id	Variant_label	Output time	Experimental design
amip	r1i1p1f1	1979.1–2021.11	A reference experiment, the model integration starts from January 1, 1976. All external forcing factors, including greenhouse gases, solar irradiance, ozone and aerosols, are specified as their historical values. And the SST and sea-ice concentration prescribed as the observed values. Export data from January 1, 1979 to December 15, 2021 for analysis.
amip_NMO	r1i1p1f1	1979.1–2021.11	The dynamical perturbation experiment, the height of the topography in the MP and its surrounding regions is modified. The topography above 500 m in the MP and its surrounding regions was set to 500 m.
amip_NS_MO	r1i1p1f1	1979.1–2021.11	The thermal perturbation experiment, which removes the surface sensible heating over the MP and surrounding regions at altitudes above 500 m.

Table 1. Experimental design.

this experiment, the topography height retained its original values, but the surface heating effect of the MP to the atmosphere is removed. This means that the vertical diffusion heating term from the surface to the atmosphere in regions above 500 m on and around the MP is set to zero. The output variables time is the same as other experiments.

All the external forcing fields in the experiment are set as monthly average observations according to the CMIP6 standard, including: the historical global average data of greenhouse gas concentration from Meinshausen *et al.*[38]. were used; the solar radiation forcing was derived from the solar activity data set of Matthes *et al.*[39].; the ozone concentration is based on the CCMI historical forcing database (from http://blogs.reading.ac.uk/ccmi/forcing-databases-in-support-of-cmip6/); the SST and Sea Ice data refer to the AMIP data set of the program for Climate Model Diagnosis & Intercomparison (PCMDI, available at https://esgf-node.llnl.gov/projects/esgf-llnl/); the aerosol mass concentration was calculated using the NCAR Community Atmosphere Model with Chemistry (CAM-Chem)[40], covering five components: sulfate, sea salt, black carbon, organic carbon and dust; land use data were set as climatological mean[41].

Data Records

The datasets set generated by our numerical simulation experiment has a global spatial resolution of $1° \times 1°$, and spans the period from 1979 to 2021. It comprises 42 variables essential for atmospheric and climate studies, including temperature, pressure, humidity, wind speed, precipitation, and other commonly used meteorological quantities. These variables consist of 10 multi-level data (with the model's 32 vertical level) and 32 single-level data. The datasets cover different time scales, such as 41 monthly average data, 24 daily average data, 8 six-hourly transient data, and 2 one-hourly data. Detailed variable names, abbreviations, units and other related information can be obtained in Supplementary Table 1.

The monthly data of this datasets can be publicly available on https://doi.org/10.26050/WDCC/C6sGMCASFF[42], and the daily and hourly data can be publicly available on https://doi.org/10.12392/IAP-Earthlab.2025.001[43]. These data are provided in "NetCDF" format and enabling compatibility with standard analysis tools such as Python, NCL, MATLAB, and others. The data file of the dataset is named "CMIP6_supplemental GMMIP CAS FGOALS-f3-L xxxx r1i1p1f1 Amon yyyy", where "CMIP6_supplemental GMMIP CAS FGOALS-f3-L" denotes that this dataset is a supplementary experimental dataset of CMIP6-GMMIP, using the FGOALS-f3-L numerical simulation model of the Chinese Academy of Sciences. The "xxxx" represents the name of the experiment (e.g., amip), "Amon" indicates monthly data frequency, and "yyyy" represents the abbreviation of the variable name (referenced to Supplementary Table 1 for full names). For example, the data named "CMIP6_supplemental GMMIP CAS FGOALS-f3-L amip r1i1p1f1 Amon cl" contains the monthly mean cloud cover percentage (cl) from the amip experiment. Each monthly data file encompasses the period from January 1979 to November 2021.

Technical Validation

In this section, the model's basic performance is validated by comparing with the observational data, and the simulation results of the model will be evaluated across diverse time scales. It is mainly to compare the amip experiment with the observation data to verify the accuracy and reliability of the data set. The amip_NMO and amip_NS_MO will be basically described and not further analyzed.

The observational datasets used include the *Climatic Research Unit gridded Time Series* (*CRU TS*, openly available at https://www.uea.ac.uk/groups-and-centres/climatic-research-unit/data)[44,45], a high-resolution global long-term climate dataset that developed and maintained by the *Climatic Research Unit (CRU)* at the University of East Anglia. This dataset is primarily based on meteorological observations from stations around the world. The data include various meteorological elements such as temperature, precipitation, humidity, wind speed, cloud amount, etc. The precipitation data used in this study are from the *Global Precipitation Climatology Project* (*GPCP*, openly available at https://climatedataguide.ucar.edu/climate-data/gpcp-monthly-global-precipitation-climatology-project)[46,47] dataset, which is an international research project that provides a global precipitation dataset. In the scientific community, the *GPCP* Monthly Analysis (Version 2.3) is widely used for analyzing regional and global precipitation changes and trends at climate scale. The study also used atmospheric circulation data from the *European Centre for Medium-Range Weather Forecasts (ECMWF) Reanalysis version 5* (*ERA5*, openly available at https://cds.climate.copernicus.eu/datasets)[48] dataset. The observational data used in this study are all monthly data from 1979 to 2021, and have been bilinearly

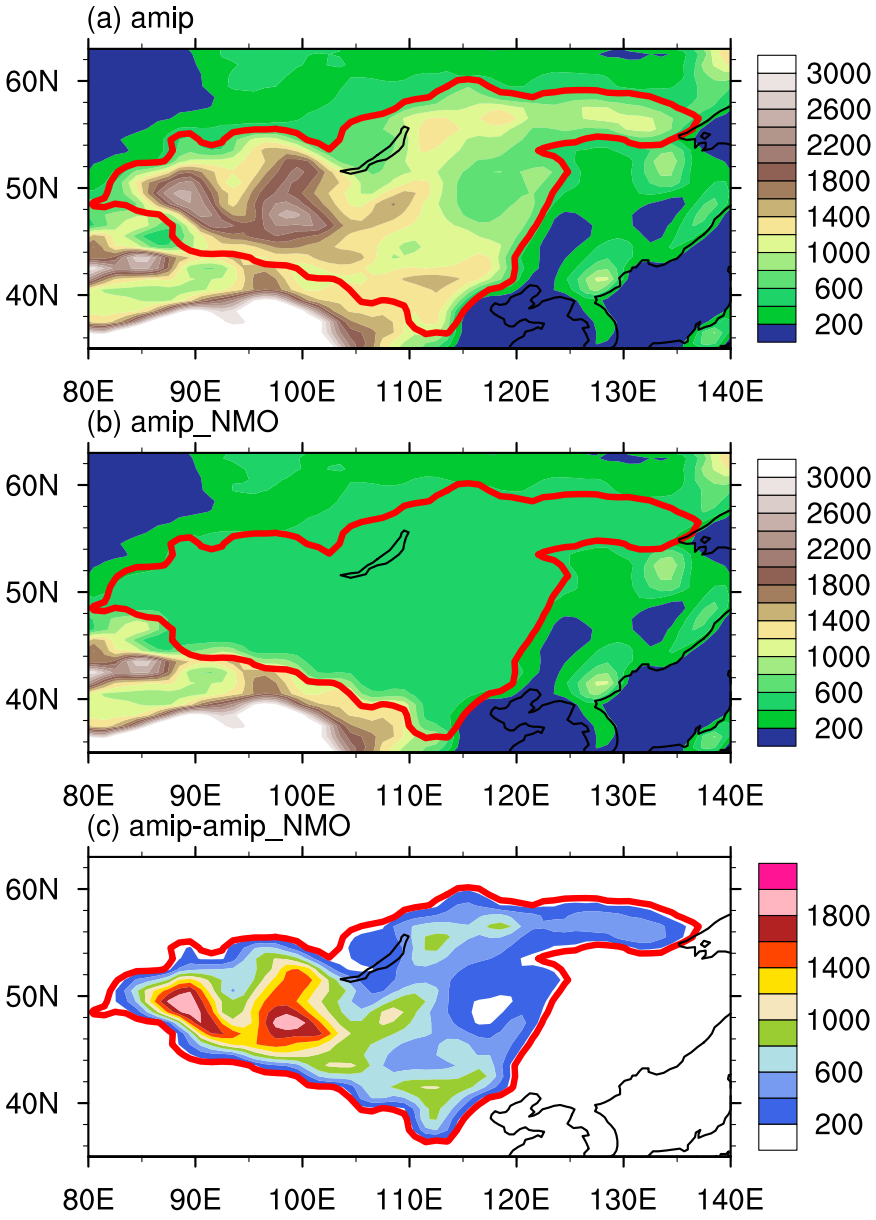

Fig. 1 Topographic heights of the experiments (unit: m). (**a**) the control group experiment (amip), (**b**) the experiment of removing the MP (amip_NMO), and (**c**) the differences between amip experiment and amip_NMO experiment (the thick red line is the region where the orography is removed).

interpolated to a resolution of 1° × 1°, consistent with the model resolution, to facilitate analysis and comparison between observations and experimental results.

First, we show the two topography forcings for the simulation (Fig. 1). In the amip run, the terrain within the model remains unchanged, so the elevation height represents the actual height values. The maximum height is around 3000 m, mainly concentrated in the western regions of the MP (Fig. 1a). In the amip_NMO run, according to the experimental design, areas in the MP and its surrounding regions with terrain heights exceeding 500 m are set to 500 m (Fig. 1b). The topography difference between the amip run and the amip_NMO run is shown in Fig. 1c. In the high-altitude areas of the MP, the differences are most pronounced, especially in the red regions depicted in the figure, where the height change exceeds 1800 m, whereas low-altitude areas (blue regions) exhibit relatively smaller changes in height.

In the no sensible heating run, the vertical heating transfer from the surface to the atmosphere at a height exceeding 500 m above the MP and its surrounding regions are set to zero. Figure 2 shows the climatological average (from January 1979 to November 2021) of the vertical diffusion heating from the surface (Temperature Vertical Diffusion, DTV) of the three experiments. In the amip experiment, neither the terrain nor the thermal parameters were modified, thus reflecting the actual topography of the MP and its global impact on the climate. From the distribution of DTV, it can be observed that significant differences in the MP at different altitude regions, indicating that its terrain height and thermal effects have an impact on the regional climate. There is

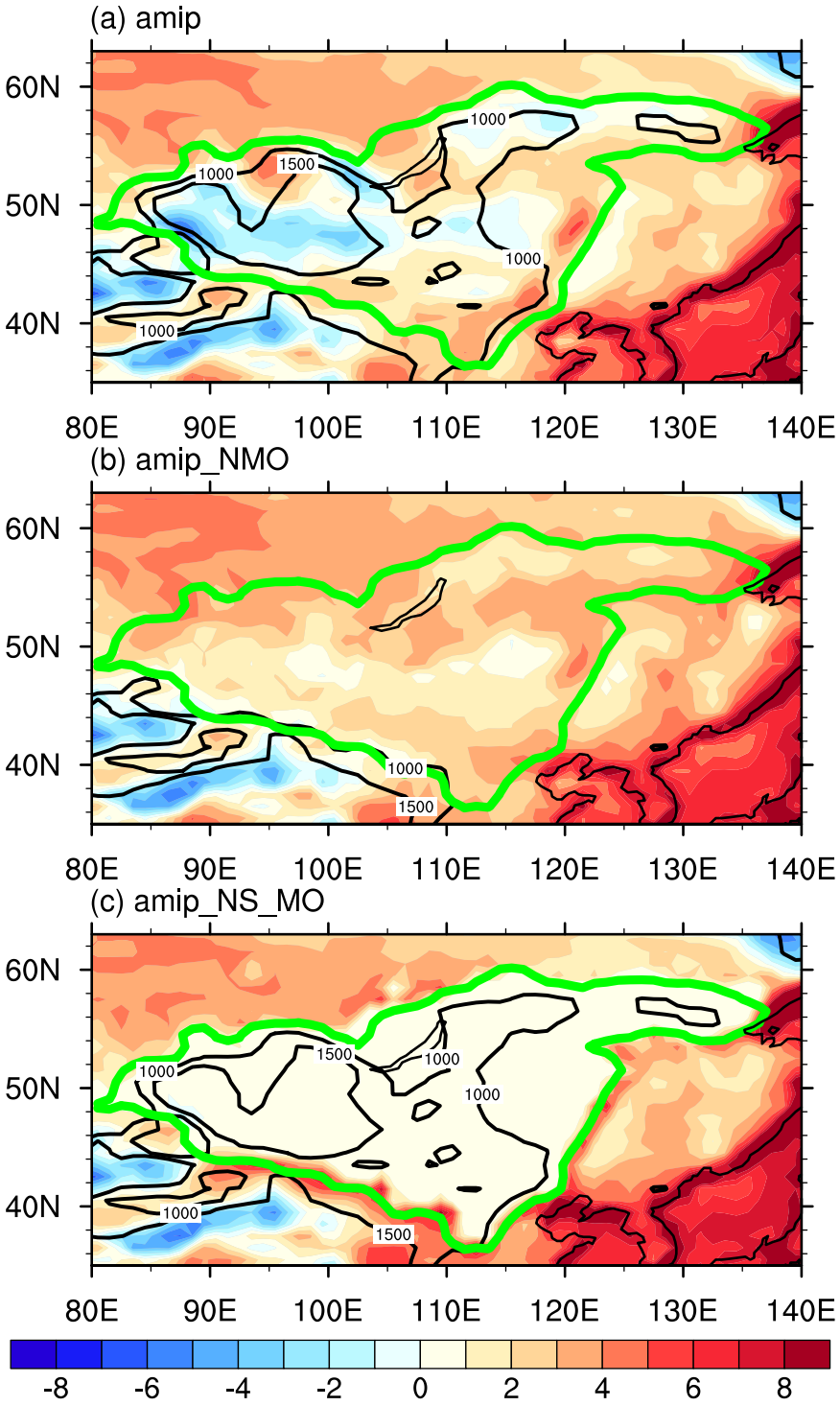

Fig. 2 Climatological mean (1979–2021) of surface vertical diffusion heating of the experiments. (unit: K Day^{-1}). (**a**) amip, (**b**) amip_NMO, and (**c**) the thermal perturbation experiment (amip_NS_MO) (the black contour represents topographic heights (unit: m) and the thick green contour is the experimental region).

a pronounced cooling effect (blue regions) in the high-altitude areas of the MP, while lower altitude regions exhibit heating status (Fig. 2a).

In the amip_NMO run, the topography height of the MP was reduced. This implies that when the airflows pass over the MP, it is no longer affected by orographic lifting, and the uplifted thermal and dynamic disturbances are significantly weakened (Fig. 2b). Compared to the amip experiment, after removing the topography, the cooling effect in the MP is significantly weakened. Instead, there is a more uniform distribution of DTV. In the amip_NS_MO run, the topography of the MP was retained, yet the vertical heating from the surface to the atmosphere was removed. This setup simulates where the thermal influence of the MP on the atmosphere is

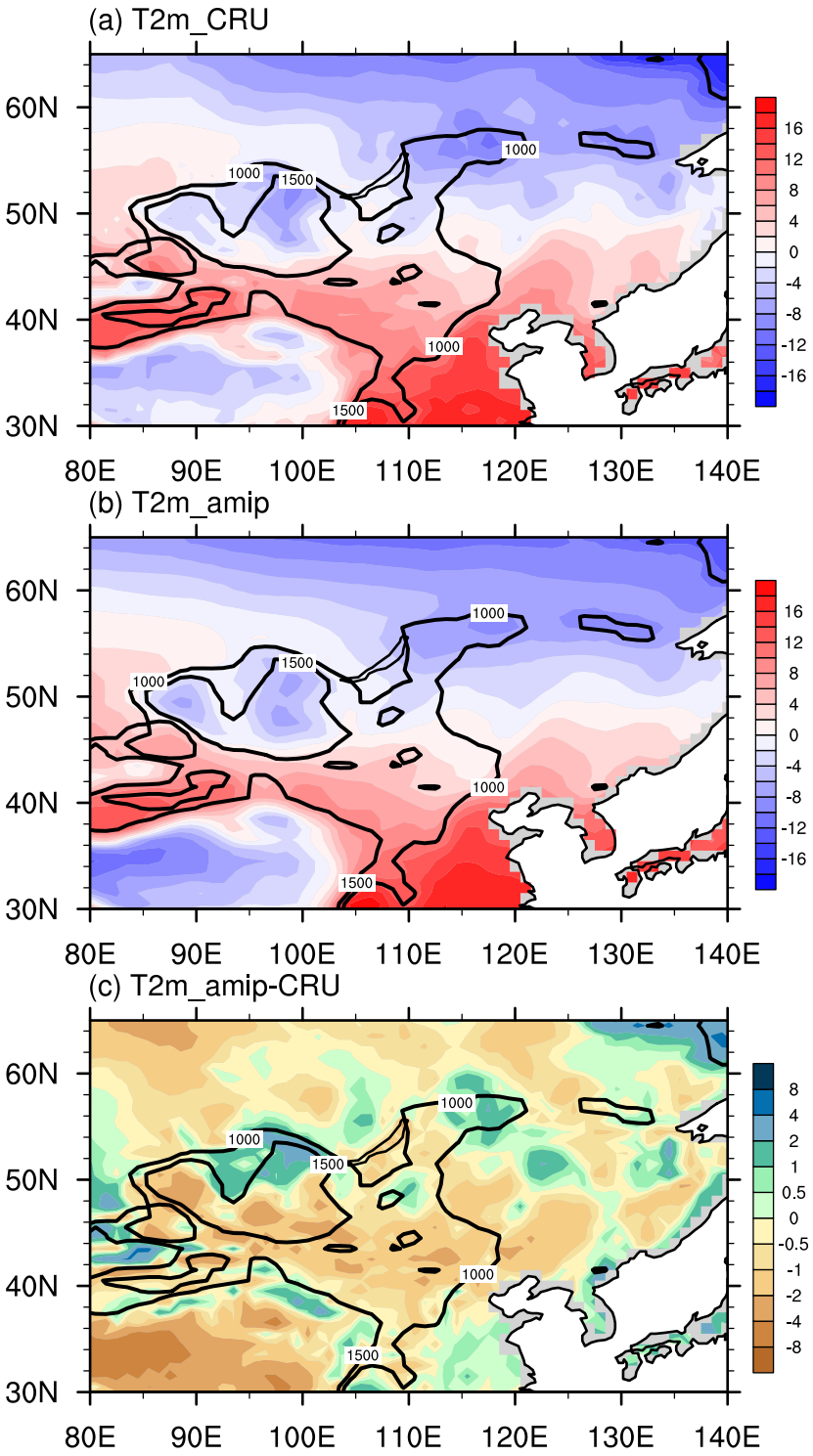

Fig. 3 Climatological mean of Two meters temperature (unit: °C). (**a**) CRU TS, (**b**) amip, and (**c**) the differences between amip and CRU TS (the black contour represents topographic heights (unit: m)).

weakened. It is clearly evident that the DTV within the experimental region is zero (Fig. 2c), thereby confirming the correctness of our sensitivity experiments.

The two-meter air temperature (T2m) is one of the crucial evaluation metrics. Here, we show a spatial pattern comparison between the T2m in the *CRU TS dataset* and the T2m output from the amip experiment. Figure 3 shows the basic spatial characteristics of the climatological mean (1979–2021) T2m. The distribution of T2m in both the observed dataset *CRU TS* (Fig. 3a) and the amip experiment (Fig. 3b) are generally similar. Both show a cold region in the north of the MP and a warm region in the south, indicating that the model has

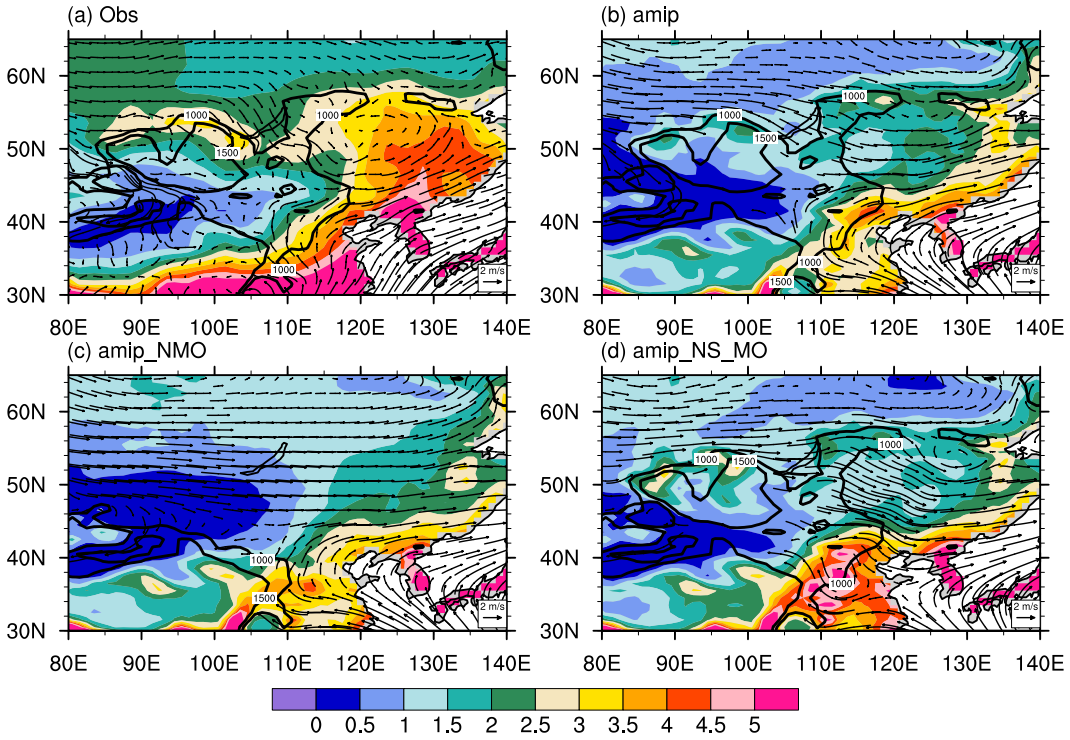

Fig. 4 Climatological JJA mean precipitation (shaded; unit: mm day^{-1}), and 850 hPa wind of ERA5 (arrows; unit: m s^{-1}). (**a**) GPCP, (**b**) amip, (**c**) amip_NMO, and (**d**) amip_NS_MO (the black contour represents topographic heights (unit: m)).

well simulated the basic pattern of T2m distribution. In some local regions, particularly in areas with complex terrain and high altitude, the simulation results may exhibit certain biases.

The difference of T2m between amip and *CRU TS* (Fig. 3c) shows a spatial discrepancy in the bias, particularly over the MP and its adjacent regions. There are notable temperature biases and characteristic differences across different regions. Major cold biases are observed near the TP and southern regions of the MP, as well as mid-latitudes of the Asian continent around 40–50°N. Positive biases are observed on the northern side of the MP and at latitudes between 50–60°N in Asia. The model overestimates the extent of warm regions in Central Asia and northern China, while underestimating the cooling effect in the northern part of the MP. The cause of the cold bias in MP is similar as the cold bias in TP in the FGOALS-f3-L. Wu *et al.*[49]., found that the model underestimated the annual mean temperature of the TP, primarily attributable to the negative contribution of surface albedo feedback (SAF). An overestimation of the high albedo associated with snow or ice cover in high-altitude regions likely leads to reduced absorption of solar shortwave radiation at the surface, consequently lowering surface temperatures. Located within the central transition zone of the plateau, the MP region exhibits heightened sensitivity to surface albedo and shortwave radiation. In this area, the negative SAF contribution is not fully compensated by other energy budget components, resulting in the underestimation of 2m air temperatures near MP.

The dynamic and thermal forcing effects of the MP's topography may change the paths and intensities of atmospheric circulation[50], and further influence the transportation and convergence of water vapor[51]. Therefore, an evaluation of precipitation and 850 hPa wind simulation is also necessary. Observed precipitation data were sourced from the *GPCP dataset*, while 850 hPa wind were obtained from the *ERA5* dataset. Here we show the climatological distribution characteristics of boreal summer (June-July-August, JJA) mean precipitation and 850 hPa wind, as well as the climate mean responses of MP dynamical and thermal effects on the Asian Summer Monsoon in Fig. 4. Comparing the observational data (Fig. 4a) with the amip experimental results (Fig. 4b), the model demonstrates a good ability to simulate precipitation distribution characteristics, effectively reproducing the fundamental patterns of precipitation in East Asia. The simulation of the 850 hPa wind also largely reproduces the features of the monsoon system, exhibiting a circulation pattern dominated by westerly winds that similar to those observed, as well as a relatively strong southwest monsoon flow along the East Asian coastal region. This monsoon flows to southeastern China and brings a large amount of water vapor, thereby enhancing precipitation.

While there are also some biases in the model. The precipitation in southern China, North China Plain and Korean Peninsula is lower than the observation, the location of the extreme precipitation area is slightly offset. Additionally, the extent of the southwest monsoon along the coastal regions is relatively limited. He *et al.*[52], revealed that the FGOALS-f3-L model exhibits a systematic precipitation bias characterized by overestimation over oceanic regions and underestimation over land. The causes can be summarized as the following mechanisms: an imbalance in water vapor transport arises from excessive horizontal water vapor advection and

layers (from bottom to top)	a	b
1	0	0.996115029
2	0.003162475	0.984234989
3	0.010152949	0.966544986
4	0.018579246	0.945169985
5	0.028675733	0.919475019
6	0.040713709	0.888715029
7	0.054981098	0.852069974
8	0.071763836	0.808664978
9	0.091316633	0.757634997
10	0.113815531	0.698194981
11	0.139284119	0.629764974
12	0.167481646	0.552150011
13	0.197736159	0.465815008
14	0.228660807	0.372370005
15	0.257687211	0.275545001
16	0.280738354	0.182115003
17	0.292708129	0.101044998
18	0.288511932	0.04095
19	0.263399184	0.008555
20	0.221711785	0
21	0.178474441	0
22	0.141757995	0
23	0.111005813	0
24	0.085623093	0
25	0.064995073	0
26	0.048505057	0
27	0.035527151	0
28	0.02537718	0
29	0.017353408	0
30	0.010987443	0
31	0.006093011	0
32	0.0025	0

Table 2. Hybrid level coefficients of CAS FGOALS-f3-L atmospheric component.

underestimated vertical dynamic advection, leading to insufficient column-integrated water vapor convergence which thereby weakens monsoon precipitation[53,54]; deficiencies in cloud-radiation feedback occur, where low cloud cover over the monsoon trough region suppresses convective activity, ultimately reducing precipitation[55]; the uncertainty of cloud microphysical parameterization affects the spatial and temporal distribution of precipitation, and the spatial resolution of $1° \times 1°$(improving the resolution can improve the accuracy) is still one of the reasons of simulation bias in amip run[56].

In the amip_NMO experiment (Fig. 4c), it can be observed that there are significant reductions in precipitation over northern MP and northern China. The region of heavy rainfall over the North China Plain has shifted southward. Changes in wind field are also evident, with the MP's topography exerting a notable blocking and guiding effect on the westerly winds. This results in a weakening of the southwest monsoon flow, leading to reduced moisture transport into southeastern China, thereby affecting precipitation. These findings indicate that the orographic features of the MP significantly influence precipitation distribution by altering atmospheric circulation pathways and intensities. In the amip_NS_MO experiment (Fig. 4d), precipitation is notably enhanced over northern MP, the East Asian coastal region. And the North China Plain, where a significant band of heavy rainfall forms. Furthermore, there is an increase in the intensity of the 850 hPa wind, particularly along the critical moisture transport pathways associated with the East Asian monsoon.

Here, we evaluate the accuracy of the model data based on the circulation situation and trough ridge situation in the Northern Hemisphere. Northern Hemisphere winter (December–January–February, DJF) 500 hPa geopotential height latitude anomaly and winds in Fig. 5. In the *ERA5* (Fig. 5a) and amip experiment (Fig. 5b), it can be clearly observed that there is a clear "one trough and one ridge" situation in the Northeast Hemisphere, as well as the existence of a strong East Asian trough. It shows that the simulation ability of the model is excellent. There is an anticyclone in the south of the westerly jet stream belt in the middle latitudes of the western Pacific in eastern Asia. A large-scale circulation model dominated by the westerlies. The westerly belt is obvious in the mid-latitude region (40°N - 60°N), showing a relatively stable airflow, flowing along the trend of the geopotential height contour. However, there are some differences in the ridge strength and flow field details of the model in some areas. It is mainly reflected in the fact that the amip experiment underestimates the strength of the ridge in western North America and Europe, especially in the western region of Europe, which is slightly weaker.

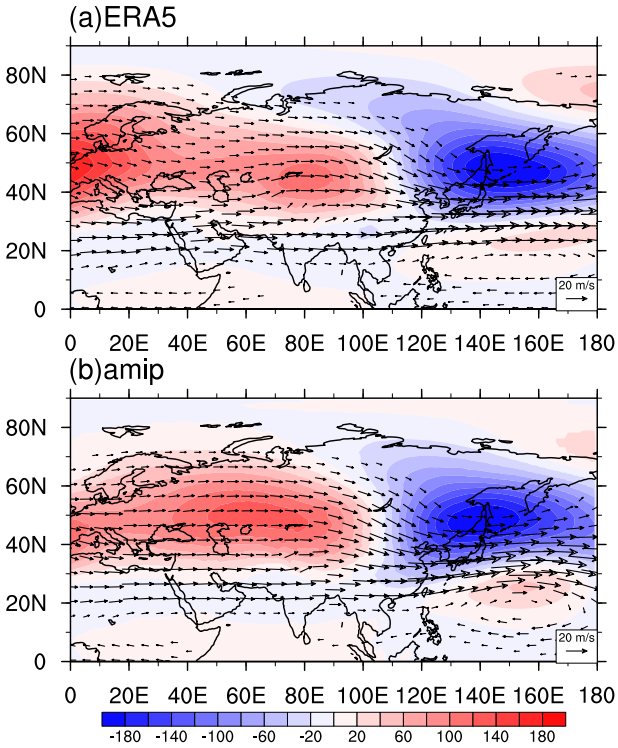

Fig. 5 Climatological DJF mean 500 hPa latitude anomaly of geopotential height (0–180°E, shaded; unit: dagpm) and wind (arrows; unit: m s^{-1}). (**a**) ERA5 and (**b**) amip.

These results show that the model can better reproduced the basic pattern of the atmospheric circulation and could well capture the large-scale dynamics involved by orographical perturbations. These datasets will help to understand the contribution of the MP to the mid-high latitude monsoon circulation, winter cold wave and even extreme events, and also help to better understand the impact of Asian topography on the global monsoon system.

Usage Notes

The initial atmospheric model grid utilizes a cube-sphere grid system with a C96 resolution. Comprising 6 tiles, it exhibits irregularity in the horizontal plane. In compliance with the stipulations of CMIP6, we combine and interpolate these tiles onto the global latitude-longitude grid, attaining a nominal resolution of 1° for public accessibility via the first-order conservative interpolation technique.

For those users who are required to analysis the pressure layer datasets, we supply the hybrid level "A" coefficient (a) and the hybrid level "B" coefficient at the mid-point level (b) in Table 2 for interpolation from model layers to pressure layers. Subsequently, the pressure can be obtained through the following formula:

$$P(i, j, k) = A_k P_0 + B_k P_s(i, j) \quad (1)$$

Among them, $P(i, j, k)$ denotes the pressure required by the model, A_k corresponds to a, P_0 is equal to 1000 hPa, B_k is b, $P_s(i, j)$ represents the surface pressure, i, j, k respectively stand for the longitude index, the latitude index and the vertical layer index.

Code availability

The code of bulking download daily and hourly data is available at https://github.com/xunuo-xx/MP-model-dataset/blob/main/get_FGOALS_data.py. The codes of drawing figures in the article can be obtained from https://github.com/xunuo-xx/MP-model-dataset.

Received: 17 January 2025; Accepted: 17 July 2025;
Published online: 25 July 2025

References

1. Queney, P. The problem of air flow over mountains: A summary of theoretical studies. *Bull. Amer. Meteor. Soc.* **29**(1), 16–26, https://doi.org/10.1175/1520-0477-29.1.16 (1948).
2. Abe, M., Kitoh, A. & Yasunari, T. An evolution of the Asian summer monsoon associated with mountain uplift—Simulation with the MRI atmosphere-ocean coupled GCM. *J. Meteor. Soc. Japan* **81**(5), 909–933, https://doi.org/10.2151/jmsj.81.909 (2003).
3. Okajima, H. & Xie, S. P. Orographic effects on the northwestern Pacific monsoon: Role of air-sea interaction. *Geophys. Res. Lett.* **34**(21), L21708, https://doi.org/10.1029/2007GL032206 (2007).

4. Zhou, X. J., Zhao, P., Chen, J. M., Chen, L. X. & Li, W. L. Impacts of thermodynamic processes over the Tibetan Plateau on the Northern Hemispheric climate. *Science in China Series D: Earth Sciences* **52**(11), 1679–1693, https://doi.org/10.1007/s11430-009-0194-9 (2009).
5. Boos, W. & Kuang, Z. Dominant control of the South Asian monsoon by orographic insulation versus plateau heating. *Nature* **463**, 218–222, https://doi.org/10.1038/nature08707 (2010).
6. Wu, G. & Liu, Y. Impacts of the Tibetan plateau on Asian climate. *Meteorol Monogr* **56**, 1–29, https://doi.org/10.1175/amsmonographs-d-15-0018.1 (2016).
7. Lu, M. *et al*. Possible effect of the Tibetan Plateau on the "upstream" climate over West Asia, North Africa, South Europe and the North Atlantic. *Clim Dyn* **51**, 1485–1498, https://doi.org/10.1007/s00382-017-3966-5 (2018).
8. Liu, Y., Li, Y., Huang, J., Zhu, Q. & Wang, S. Attribution of the Tibetan Plateau to northern drought. *Natl Sci Rev* **7**, 489–492, https://doi.org/10.1093/nsr/nwz191 (2019).
9. Liu, Y. *et al*. Land–atmosphere–ocean coupling associated with the Tibetan Plateau and its climate impacts. *Natl Sci Rev* **7**, 534–552, https://doi.org/10.1093/nsr/nwaa011 (2020).
10. Hu, W. T., Duan, A., Li, Y. & He, B. The Intraseasonal Oscillation of Eastern Tibetan Plateau Precipitation in Response to the Summer Eurasian Wave Train. *J. Climate* **29**, 7215–7230, https://doi.org/10.1175/JCLI-D-15-0620.1 (2016).
11. He, B. *et al*. Model sensitivity of Tibetan Plateau surface potential vorticity and the Asian summer monsoon system to Asian orographic perturbation in FGOALS-f2. *Fundamental Research*. https://doi.org/10.1016/j.fmre.2023.08.013 (2023).
12. He, B., Liu, Y., Wu, G., Wang, Z. & Bao, Q. The role of air–sea interactions in regulating the thermal effect of the Tibetan–Iranian Plateau on the Asian summer monsoon. *Climate Dynamics* **52**, 4227–4245, https://doi.org/10.1007/s00382-018-4377-y (2019).
13. Wu, G. *et al*. The influence of mechanical and thermal forcing by the Tibetan plateau on Asian climate. *J Hydrometeorol* **8**, 770–789, https://doi.org/10.1175/jhm609.1 (2007).
14. Wu, G. *et al*. Thermal controls on the Asian summer monsoon. *Sci Rep* **2**, 404, https://doi.org/10.1038/srep00404 (2012).
15. He, B., Sheng, C., Wu, G., Liu, Y. & Tang, Y. Quantification of seasonal and interannual variations of the Tibetan Plateau surface thermodynamic forcing based on the potential vorticity. *Geophysical Research Letters* **49**(5), e2021GL097222, https://doi.org/10.1029/2021GL097222 (2022).
16. Molnar, P., Boos, W. R. & Battisti, D. S. Orographic Controls on Climate and Paleoclimate of Asia: Thermal and Mechanical Roles for the Tibetan Plateau[J]. *Annual Review of Earth & Planetary Sciences* **38**(1), 77–102, https://doi.org/10.1146/annurev-earth-040809-152456 (2010).
17. Jiang, L. *et al*. Climate Variability and Change on the Mongolian Plateau: Historical Variation and Future Predictions. *Climate Research*, **67**(1), 1–14, JSTOR. https://www.jstor.org/stable/24896542 (2016).
18. Shi, Z. *et al*. Impact of Mongolian Plateau versus Tibetan Plateau on the westerly jet over North Pacific Ocean. *Clim Dyn* **44**, 3067–3076, https://doi.org/10.1007/s00382-014-2217-2 (2015).
19. Sha, Y. *et al*. Distinct impacts of the Mongolian and Tibetan Plateaus on the evolution of the East Asian monsoon[J]. *Journal of Geophysical Research Atmospheres* **120**(10), 4764–4782, https://doi.org/10.1002/2014JD022880 (2015).
20. Xie, Z. *et al*. Intraseasonal transition of Northern Hemisphere planetary waves and the underlying mechanism during the abrupt-change period of early summer. *Climate Dynamics* **59**, 1435–1449, https://doi.org/10.1007/s00382-021-06048-5 (2022).
21. Lin, Z., Bueh, C. & He, B. Mechanical and thermal effects of Asian topography on northern East Asian low. *Clim Dyn* **62**, 447–458, https://doi.org/10.1007/s00382-023-06928-y (2024).
22. White, R. H., Battisti, D. S. & Sheshadri, A. Orography and the Boreal Winter Stratosphere: The Importance of the Mongolian Mountains [J]. *Geophysical Research Letters* https://doi.org/10.1002/2018GL077098 (2018).
23. He, B. *et al*. CAS FGOALS-f3-L Model Datasets for CMIP6 GMMIP Tier-1 and Tier-3 Experiments. *Adv. Atmos. Sci.* **37**, 18–28, https://doi.org/10.1007/s00376-019-9085-y (2020).
24. Zhou, L. *et al*. Global energy and water balance: Characteristics from Finite-volume Atmospheric Model of the IAP/LASG (FAMIL1). *J. Adv. Model. Earth Syst.* **7**, 1–20, https://doi.org/10.1002/2014ms000349 (2015).
25. Bao, Q. *et al*. Outlook for El Nino and the Indian Ocean Dipole in autumn-winter 2018–2019. *Chinese Science Bulletin* **64**, 73–78, https://doi.org/10.1360/N972018-00913 (2019).
26. Li, J. X. *et al* Evaluation of FAMIL2 in simulating the climatology and seasonal-to-interannual variability of tropical cyclone characteristics, *J. Adv. Model. Earth Syst*. https://doi.org/10.1029/2018MS001506 (2019).
27. Wu, G. X., Liu, H., Zhao, Y. & Li, W. A nine-layer atmospheric general circulation model and its performance. *Adv. Atmos. Sci.* **13**(1), 1–18, https://doi.org/10.1007/bf02657024 (1996).
28. Bao, Q. *et al*. An introduction to the coupled model FGOALS1. 1-s and its performance in East Asia. *Adv. Atmos. Sci.* **27**(5), 1131–1142, https://doi.org/10.1007/s00376-010-9177-1 (2010).
29. Bao, Q. *et al*. The Flexible Global Ocean-Atmosphere-Land system model, Spectral Version 2: FGOALS-s2. *Adv. Atmos. Sci.* **30**, 561–576, https://doi.org/10.1007/s00376-012-2113-9 (2013).
30. Liu, H., Lin, P., Yu, Y. & Zhang, X. The baseline evaluation of LASG/IAP climate system ocean model (LICOM) version 2. *Acta Meteorologica Sinica* **26**(3), 318–329, https://doi.org/10.1007/s13351-012-0305-y (2012).
31. Hunke, E. C., Lipscomb, W. H., Turner, A. K., Jeffery, N. & Elliott, S. CICE: the Los Alamos Sea Ice Model Documentation and Software User's Manual Version 4.1 LA-CC-06-012. T-3 Fluid Dynamics Group, Los Alamos National Laboratory, 675 (2010).
32. Bretherton, C. S. & Park, S. new moist turbulence parameterization in the community atmosphere model. *J. Climate* **22**(12), 3422–3448, https://doi.org/10.1175/2008JCLI (2009).
33. Wang, X. C. & Zhang, M. H. Vertical velocity in shallow convection for different plume types. *Journal of Advances in Modeling Earth Systems* **6**(2), 478–489, https://doi.org/10.1002/2014MS000318 (2014).
34. Lin, Y. L., Farley, R. D. & Orville, H. D. Bulk parameterization of the snow field in a cloud model. *J. Climate Appl. Meteor.* **22**(6), 1065–1092, 10.1175/1520-0450(1983)022<1065:BPOTSF>2.0.CO;2 (1983).
35. Harris, L. M. & Lin, S.-J. Global-to-regional nested grid climate simulations in the GFDL high resolution atmospheric model. *J. Climate* **27**(13), 4890–4910, https://doi.org/10.1175/JCLI-D-13-00596.1 (2014).
36. Xu, K. M. & Randall, D. A. A semiempirical cloudiness parameterization for use in climate models. *J. Atmos. Sci* **53**(21), 3084–3102, 10.1175/1520-0469(1996)053<3084:ASCPFU>2.0.CO;2 (1996).
37. Palmer, T. N., Shutts, G. J. & Swinbank, R. Alleviation of a systematic westerly bias in general circulation and numerical weather prediction models through an orographic gravity wave drag parametrization. *Quart. J. Roy. Meteor. Soc.* **112**(474), 1001–1039, https://doi.org/10.1002/qj.49711247406 (1986).
38. Meinshausen, M. and Coauthors. Historical greenhouse gas concentrations for climate modelling (CMIP6). *Geoscientific Model Development* **10**, 2057–2116, https://doi.org/10.5194/gmd-10-2057-2017 (2017).
39. Matthes, K. and Coauthors. Solar forcing for CMIP6 (v3.2). *Geoscientific Model Development* **10**(6), 2247–2302, https://doi.org/10.5194/gmd-10-2247-2017 (2017).
40. Lamarque, J.-F. and Coauthors. CAM-chem: Description and evaluation of interactive atmospheric chemistry in the community earth system model. *Geoscientific Model Development* **5**(2), 369–411, https://doi.org/10.5194/gmd-5-369-2012 (2012).
41. Hurtt, G. C. and Coauthors. Harmonization of land-use scenarios for the period 1500–2100: 600 years of global gridded annual land-use transitions, wood harvest, and resulting secondary lands. *Climatic change* **109**(1–2), 117, https://doi.org/10.1007/s10584-011-0153-2 (2011).

42. He, Bian. CMIP6_supplemental GMMIP CAS FGOALS-f3-L. World Data Center for Climate (WDCC) at DKRZ. https://doi.org/10.26050/WDCC/C6sGMCASFF (2024).
43. Xu, N. *et al*. Model datasets of orographical perturbation experiments for the Mongolian plateau by using CAS FGOALS-f3-L. IAP-Earthlab. https://doi.org/10.12392/IAP-Earthlab.2025.001 (2025).
44. Jones, P. D. & Moberg, A. Hemispheric and Large-Scale Surface Air Temperature Variations: An Extensive Revision and an Update to 2001. *J. Climate* **16**, 206–223, 10.1175/1520-0442(2003)016<0206:HALSSA>2.0.CO;2 (2003).
45. Harris, I. *et al*. Version 4 of the CRU TS monthly high-resolution gridded multivariate climate dataset. *Sci Data* **7**, 109, https://doi.org/10.1038/s41597-020-0453-3 (2020).
46. Adler, R. & Coauthors Global Precipitation Climatology Project (GPCP) Climate Data Record (CDR), Version 2.3 (Monthly). https://doi.org/10.7289/V56971M6 (2016).
47. Adler, R. F. *et al*. The Global Precipitation Climatology Project (GPCP) Monthly Analysis (New Version 2.3) and a Review of 2017 Global Precipitation. *Atmosphere* **9**(4), 138, https://doi.org/10.3390/atmos9040138 (2018).
48. Hersbach, H. *et al*. Complete ERA5 from 1940: Fifth generation of ECMWF atmospheric reanalyses of the global climate. Copernicus Climate Change Service (C3S) Data Store (CDS). https://doi.org/10.24381/cds.143582cf (Accessed on DD-MMM-YYYY) (2017).
49. Wu, Y. *et al*. Analysis of surface temperature bias over the Tibetan plateau in the CAS FGOALS-f3-L model. *Atmospheric Oceanographic Sciences Library* **14**(1), 100012, https://doi.org/10.1016/j.aosl.2020.100012 (2021).
50. Wang, W. & Feng, Z. Holocene moisture evolution across the Mongolian Plateau and its surrounding areas: A synthesis of climatic records. *Earth-Science Reviews* **122**, 38–57, https://doi.org/10.1016/j.earscirev.2013.03.005 (2013).
51. Hu, W. T., She, D. X., Xia, J., He, B. & Hu, C. Dominant patterns of dryness/wetness variability in the Huang-Huai-Hai River Basin and its relationship with multiscale climate oscillations. *Atmospheric Research* **247**, 105148, https://doi.org/10.1016/j.atmosres.2020.105148 (2021).
52. He, B. *et al*. CAS FGOALS-f3-L Model Datasets for CMIP6 Historical Atmospheric Model Intercomparison Project Simulation. *Advances in Atmospheric Sciences* **36**(8), 771–778, https://doi.org/10.1007/s00376-019-9027-8 (2019).
53. Huang, X., Zhou, T. J., Wu, B. & Chen, X. L. South Asian Summer Monsoon Simulated by Two Versions of FGOALS Climate System Model: Model Biases and Mechanisms. *Chinese Journal of Atmospheric Sciences* **43**(2), 437–455, https://doi.org/10.3878/j.issn.1006-9895.1805.18131 (2019).
54. Tang, Y. *et al*. The climate variability in global land precipitation in FGOALS-f3-L: A comparison between GMMIP and historical simulations. *Atmospheric and Oceanic Science Letters* **13**(6), 559–567, https://doi.org/10.1080/16742834.2020.1776088 (2020).
55. Wang, L. *et al*. LASG Global AGCM with a Two-moment Cloud Microphysics Scheme: Energy Balance and Cloud Radiative Forcing Characteristics. *Adv. Atmos. Sci.* **36**, 697–710, https://doi.org/10.1007/s00376-019-8196-9 (2019).
56. He, X. Y. *et al*. The sensitivity of the Asian summer monsoon simulation to horizontal resolution and air-sea coupling in the FGOALS-f climate system model. *Advances in Climate Change Research* **16**, 44–57, https://doi.org/10.1016/j.accre.2025.01.008 (2025).

Acknowledgements

This work was jointly supported by the National Natural Science Foundation of China (grant nos. 42288101, 42475020, 42175074) and Chinese Academy of Sciences President's International Fellowship Initiative. Grant No. 2025PVB0041. We also thank for the technical support of the National large Scientific and Technological Infrastructure "Earth System Numerical Simulation Facility" (https://cstr.cn/31134.02.EL).

Author contributions

Methodology: Nuo Xu, Bian He, Shijian Feng. Investigation: Nuo Xu, Bian He. Visualization: Nuo Xu. Supervision: Bian He, Shibo Gao. Writing-original draft: Nuo Xu, Bian He. Writing-review & editing: Nuo Xu, Bian He, Zuowei Xie, Zhongda Lin, Shijian Feng, Qing Bao, Yimin Liu, Guoxiong Wu, Kangjun Chen, Natalia Victorovna Vazaeva, Shibo Gao.

Competing interests

The authors declare no competing interests.

Additional information

Supplementary information The online version contains supplementary material available at https://doi.org/10.1038/s41597-025-05632-2.

Correspondence and requests for materials should be addressed to B.H. or S.G.